IEEE Transactions on Ultrasonics, Ferroelectrics, and Frequency Control

A Time Domain Finite Element Boundary Integration Method for Ultrasonic Non-destructive Evaluation

Journal:	*Transactions on Ultrasonics, Ferroelectrics, and Frequency Control*
Manuscript ID:	Draft
Manuscript Type:	Papers
Date Submitted by the Author:	n/a
Complete List of Authors:	Shi, Fan; Imperial College London, Mechanical Engineering Choi, Wonjae; Imperial College London, Mechanical Engineering Skelton, Elizabeth; Imperial College, Mathematics Lowe, M.J.S.; Imperial College, Mech Eng Craster, Richard; Imperial, Mathematics
Keywords:	Wave Propagation (including Elastic Waves) < Sensors, NDE, and Industrial Applications:, Material & Defect Characterization < Sensors, NDE, and Industrial Applications:, General NDE Methods < Sensors, NDE, and Industrial Applications:

A Time Domain Finite Element Boundary Integration Method for Ultrasonic Non-destructive Evaluation

F. Shi, W. Choi, E. A. Skelton, M. J. S. Lowe and R. V. Craster

Abstract

A 2D and 3D numerical modelling approach for calculating the elastic wave scattering signals from complex stress-free defects is evaluated. In this method, an efficient boundary integration across the complex boundary of the defect is coupled with a time domain finite element (FE) solver. The model is designed to simulate time domain ultrasonic non-destructive evaluation (NDE) in bulk media. This approach makes use of the hybrid concept of linking a local numerical model to compute the near field scattering behaviour and theoretical mathematical formulas for post-processing to calculate the received signals. It minimises the number of monitoring signals from the FE calculation so that the computation effort in post-processing decreases significantly. In addition, by neglecting the conventional regular monitoring box the region for FE calculation can be made smaller. In this paper, the boundary integral method is implemented in a commercial FE code, and it is validated by comparing the scattering signals with results from corresponding full FE models. The coupled method is then implemented in real inspection scenarios in both 2D and 3D, and the accuracy and the efficiency are demonstrated. The limitations of the proposed model and future works are also discussed.

I. Introduction

In Non-destructive Evaluation there is increasing interest in the ultrasonic response from defects with very complex geometry, with applications to both detecting and sizing of cracks. Developing an efficient and accurate model to simulate the time domain inspection of these defects is crucial because they predict the scattering signals and provide a direct comparison of simulation and experiment.

Analytical methodologies, such as the geometrical theory of diffraction (GTD) [1], Kirchhoff approximation [2] and their combination [3] are well known to produce fast predictions of ultrasonic responses from defects. For example, Ogilvy developed both acoustic and elastic Kirchhoff models to predict the effects on ultrasonic signals of roughness on the faces of the defect [2], [4]. However, the infinite tangential plane assumption of the Kirchhoff approximation leads to unacceptable errors when the average radius of curvature r_c is smaller than 2.12λ [5] or

F. Shi, W. Choi and M. J. S. Lowe are with the Department of Mechanical Engineering, Imperial College London

E. A. Skelton and R. V. Craster are with the Department of Mathematics, Imperial College London, London U.K.

Manuscript received May 12, 2014

when the scattering wave is near a grazing angle [6]. In addition, by ignoring multiple reflections and assuming shadowing effects, some later arrivals are missing. In fact, all analytical solutions fall short in one way or another such that they can only be applied with certain restricted ranges.

Numerical methods provide plausible alternatives but with a downside in terms of computational effort and cost. Domain meshing methods such as finite element (FE) and finite difference time domain (FDTD) methods provide alternatives to solve complex elastic wave problems because they are able to produce effectively exact solutions once the convergence condition is satisfied [7], [8]. FE is considered to be more robust and accurate for the NDE of complex defects than FDTD given that the free meshing algorithm can capture the exact shape of the defect [9]. Commercial FE packages such as Abaqus (Dassault Systemes Simulia Corp., Providence, RI) and Ansys (Ansys Inc., PA) have been widely applied in industry and are standard tools in practice. However, when dealing with wave propagation in an unbounded domain, FE suffers from high computation cost because enormous storage space is needed, especially for 3D models.

To reduce the computation effort while handling a complete inspection problem, different hybrid methods have been developed [10]–[14] in the NDE field to combine numerical and analytical results. The main idea of these methods is to model the near field scattering behaviour of the defect in a small local region, and then project the monitored values to observation points as a post-processing procedure. Finite Element Local Scattering (FELS) [10]–[12] aims at extracting scattering matrices at a single frequency, thus the FE model is run in the frequency domain. Also, a hybrid platform [13] has been developed using Auld's reciprocity principle and is capable of calculating the scattered full waveform. A rectangular monitoring box is needed for collecting the near field scattering signals, which are used to calculate measured signals. It applies a fictitious-domain method requiring a specific FE programming code by decoupling the elastodynamic equations. The corresponding 3D platform is said to be under development.

In this paper, we focus, alternatively, on time domain numerical models because we have an interest in enabling the use of qualified widely-available FE modelling procedures. Also, in the time domain, simulated waveforms including surface reflections, tip diffractions, and surface waves can be visualized and benefit real inspection techniques, such as time-of-flight diffraction. A more generic time domain hybrid method has been developed recently to calculate the complete time domain signals [14] with implementation of an existing commercial FE time explicit solver. Similar with [13], a rectangular (2D) or cubic (3D) monitoring box is placed around the defect to monitor the scattered displacements and stresses which are used for field computation.

One problem with this hybrid approach is that the 3D hybrid scheme tends to be memory intensive and time consuming when a large number of monitoring points around the defect are used for computation. Moreover, linear tetrahedral elements are normally used in 3D free meshing to solve wave scattering problems [11], [15]. However linear tetrahedral elements are known to have a low accuracy for stress analysis because the stress is a constant value everywhere within one element. The hybrid calculation may therefore require a refined mesh adjacent to the monitoring boundary of the domain.

The main motivation of this paper is to address these numerical issues by developing a time domain FE boundary integration coupled method. In this paper, we locate the monitoring points exactly at the crack surface to record

boundary values and the number of monitoring points needed is minimised. This can contribute to a significant reduction of computational effort for post-processing and a smaller region for FE calculation as well. Also, by taking advantage of the stress free boundary condition of the crack, numerical errors from the stress recovery are avoided since only values of displacement are required for post-processing.

This paper is organized as follows: Section II considers the methodology, which includes the general description of the model and the formulas for boundary integration. Section III presents a numerical verification of the proposed boundary integration. Two examples showing application to real inspection problems in 2D and 3D are presented in Section IV, and concluding remarks are made in Section V.

II. Methodology

A. Model Description

The modeling procedure in this paper makes use of the concept from hybrid methods such as [13] and in particular as developed and implemented recently in [14]. The general hybrid concept as generated in [14] to model a complete ultrasonic inspection is illustrated in Figure 1. T1 represents the transducer sending waves to the defect and T2 refers to the transducer receiving scattering waves.

The hybrid problem can be divided into three steps: transducer sending signals, defect scattering and transducer receiving signals. As described in Fig. 1, in the first step, the source field from T1 is calculated by the time domain FE model inside a small source box and the radiating waves from T1 are collected by a monitoring box around it. The hybrid scheme is applied to the monitoring signals to compute the incident wave propagating to the defect. In the second step as shown in Fig. 1, the interaction between the incident wave and the complex defect is solved by the time domain FE model inside a local defect box. The excitation of the FE model can be realized by applying specific forces to an excitation line (2D) or an excitation plane (3D) a few elements away from the defect. The values of the applied forces are given by the incident wave computed from the first step. In the third step, the scattering displacement and stress fields are collected by a monitoring box around the defect and again the hybrid scheme is implemented to calculate the scattering signal at T2. There is no restriction on the location of T2. Here we illustrate it as receiving forward-scattered signals from the defect. Alternatively, for a pulse-echo simulation, T2 could be at the same location as T1.

We broadly follow [14] by dividing into three steps as well, but with major modifications taking advantage of boundary integrals. In the first step as shown in Fig. 2, the signal sent from T1 is calculated directly from a boundary integration of the displacement of the boundary points across the transducer surface. This is also called the Rayleigh integral method to approximate the transmitter radiation. The method using a source FE box and a hybrid scheme described in Fig. 1 can also be implemented if the transducer itself is difficult to model by such a theoretical method. In the second step, the defect scattering is still calculated by the time domain FE model inside a defect box excited by an excitation line or an excitation plane. In the third step, however, unlike using a monitoring box to collect the near field scattering field, in Fig. 2 a set of monitoring nodes is now located directly at the irregular surface of the stress-free crack and only time traces of these boundary displacements are recorded.

These boundary values are integrated via a boundary integral method, which will be introduced in Section II-B, to calculate the received signals. The number of boundary points (Fig. 2) is expected normally to be much smaller than the number of nodes around the monitoring box in Fig. 1.

B. Boundary Integration

Boundary integral formulas for a stress-free crack are derived using elastic Green's theory [2] and give the scattered displacement field u_k^{sc} as:

$$u_k^{sc}(\boldsymbol{R}) = \int_S \Sigma_{ijk}(|\boldsymbol{R}-\boldsymbol{r}|)u_i(\boldsymbol{r})n_j(\boldsymbol{r})dS(\boldsymbol{r}) \tag{1}$$

Here Σ_{ijk} is the elastic stress Green's tensor, $\boldsymbol{R}$ is the vector pointing towards the far field observation point, $\boldsymbol{r}$ is the location of a surface point, u_i is the displacement field and n_j is the normal vector pointing outward from the crack surface. To solve the only unknown variable u_i, the Kirchhoff approximation [2] can be used but as mentioned in Section I, that assumes each point at the rough surface acts as an infinite tangential mirror to reflect the incident waves. The displacement u_i can thus be determined directly from the gradient of the surface point but it is then only an approximation of the real boundary displacement, with limited validity. In this paper, the time domain FE model is used to calculate u_i because it can find the exact solution once the domain is sufficiently discretized. In practice, the time traces of displacement u_i solved by FE are decoupled into frequency components with a fast Fourier transform (FFT). These frequency components are then substituted into Eq. (1) and the outputs are synthesized back into the time domain by inverse FFT.

One note is required on the use of Eq. (1): The boundary displacement u_i is the total field instead of the scattered field. Both forms are correct once the integration contour is closed because the boundary integral of the incident wave is zero. However, if only the part of the crack surface facing the source is used for integration, the displacement value in Eq. (1) needs to be the solely scattering field. In this case, it is necessary to run an additional FE model without the crack in order to calculate the purely scattered waves by extracting the incident wave field. In this paper, the total displacement field is used in order to save computation time. The consequences of this and the resulting (minor) discrepancies will be demonstrated in the next section.

With the far field assumption that $k_\alpha|\boldsymbol{R}-\boldsymbol{r}| \gg 1$ ($\alpha = p, s$) and $|\boldsymbol{R}| \gg |\boldsymbol{r}|$, Eq. (1) for a 3D model can be simplified as:

$$\boldsymbol{u}^{sc}(\boldsymbol{R}) = -ik_p \int_S \frac{e^{ik_pT}}{4\pi T}\boldsymbol{D}^p dS(\boldsymbol{r}) - ik_s \int_S \frac{e^{ik_sT}}{4\pi T}\boldsymbol{D}^s dS(\boldsymbol{r}) \tag{2}$$

Where

$$\begin{aligned} \boldsymbol{D}^p &= [(\boldsymbol{u}\cdot\boldsymbol{n})(1-\frac{2k_p^2}{k_s^2}) + \frac{2k_p^2}{k_s^2}(\boldsymbol{u}\cdot\hat{\boldsymbol{T}})(\boldsymbol{n}\cdot\hat{\boldsymbol{T}})]\hat{\boldsymbol{T}} \\ \boldsymbol{D}^s &= (\boldsymbol{n}\cdot\hat{\boldsymbol{T}})\boldsymbol{u} + (\boldsymbol{u}\cdot\hat{\boldsymbol{T}})\boldsymbol{n} - 2(\boldsymbol{u}\cdot\hat{\boldsymbol{T}})(\boldsymbol{n}\cdot\hat{\boldsymbol{T}})\hat{\boldsymbol{T}} \end{aligned} \tag{3}$$

and $\boldsymbol{T} = \boldsymbol{R} - \boldsymbol{r}$, representing the vector from a crack surface point to the far field observation point. $\hat{\boldsymbol{T}}$ denotes the unit vector of $\boldsymbol{T}$. The first part of Eq. (2) refers to the compressional scattering waves and the second part

represents the shear scattering waves. $\boldsymbol{D}^p$ and $\boldsymbol{D}^s$ are decoupled compressional and shear components of the boundary displacement.

In 3D, the surface of the crack is discretized by small triangular facets as shown in Fig. 3. The discretized 2D surface projected into the $x-y$ plane has a regular spacing of l_x in the x-axis and l_y in the y-axis. Thus Eq. (2) can be approximated as a summation of the distribution from the local numerical integration performed at each facet:

$$\boldsymbol{u}^{sc}(\boldsymbol{R}) = -ik_p \sum_{i=1}^{M} \int_{S_i} \frac{e^{ik_p T}}{4\pi T} \boldsymbol{D}^p dS_i(\boldsymbol{r}) - ik_s \sum_{i=1}^{M} \int_{S_i} \frac{e^{ik_s T}}{4\pi T} \boldsymbol{D}^s dS_i(\boldsymbol{r}) \tag{4}$$

By assuming $|\boldsymbol{R}| \gg |\boldsymbol{r}'|$, the vector between the observing point and the point at the crack surface can be approximated as:

$$\boldsymbol{R} - \boldsymbol{r} = \boldsymbol{R} - \boldsymbol{r}_i - \boldsymbol{r}' \approx |\boldsymbol{R} - \boldsymbol{r}_i| - \frac{\boldsymbol{r}' \cdot (\boldsymbol{R} - \boldsymbol{r}_i)}{|\boldsymbol{R} - \boldsymbol{r}_i|} = T_i - \boldsymbol{r}' \cdot \hat{\boldsymbol{T}}_i \tag{5}$$

Here $\boldsymbol{r}_i$ refers to the centre point of the $\boldsymbol{i}$th facet, and $\boldsymbol{r}'$ is the local coordinate within this facet. Substituting Eq. (5) into Eq. (4) yields:

$$\boldsymbol{u}^{sc}(\boldsymbol{R}) = -ik_p \sum_{i=1}^{M} \frac{e^{ik_p T_i}}{4\pi T_i} \boldsymbol{D}^p \int_{S_i} e^{-ik_p \hat{\boldsymbol{T}}_i \cdot \boldsymbol{r}'} dS_i(\boldsymbol{r}) - ik_s \sum_{i=1}^{M} \frac{e^{ik_s T_i}}{4\pi T_i} \boldsymbol{D}^s \int_{S_i} e^{-ik_s \hat{\boldsymbol{T}}_i \cdot \boldsymbol{r}'} dS_i(\boldsymbol{r}) \tag{6}$$

Eq. (6) suggests that each small triangular facet scatters a spherical wave with an amplitude defined by averaging the boundary displacement of monitoring nodes attached to the facet. The phase term represented by the integration is multiplied to give different phase variations for all facets. In 3D, the phase term can be expressed analytically by:

$$\begin{aligned} \int_{S_i} e^{-ik_\alpha \hat{\boldsymbol{T}}_i \cdot \boldsymbol{r}'} dS_i(\boldsymbol{r}) \quad = \quad & \frac{1}{(\hat{\boldsymbol{n}} \cdot \hat{\boldsymbol{z}})} \frac{-1}{ik_\alpha (\hat{T_{iy}} + B\hat{T_{iz}})} \left\{ l_x \mathrm{sinc}\left[k_\alpha (\hat{T_{ix}} - \hat{T_{iy}} + (A-B)\hat{T_{iz}}) \frac{l_x}{2} \right] \right. \\ & \left. - e^{ik_\alpha (\hat{T_{iy}} + B\hat{T_{iz}}) \frac{l_y}{2}} l_y \mathrm{sinc}\left[k_\alpha (\hat{T_{ix}} + A\hat{T_{iz}}) \frac{l_x}{2} \right] \right\} \end{aligned} \tag{7}$$

Here $\hat{\boldsymbol{n}}$ is the normal vector of the triangular facet, $\hat{\boldsymbol{z}}$ is the unit vector of the z-axis. And $A = \frac{\partial z}{\partial x}$, $B = \frac{\partial z}{\partial y}$, representing the gradient of the facet.

To compute the scattering problem in 2D, the discretization of the crack is performed by dividing the crack surface into line sections with a regular interval of l_x along the x-axis as depicted in Fig. 4. Eq. (3) and (6) can still be used here for 2D calculations but the scattering displacement $\boldsymbol{u}^{sc}$ needs to be multiplied by a scaling factor in (6) to obtain the correct value in 2D:

$$\boldsymbol{u}^{sc}(\boldsymbol{R}) = \sqrt{\frac{2i\pi}{k_p}}(-ik_p) \sum_{i=1}^{M} \frac{e^{ik_p T_i}}{4\pi\sqrt{T_i}} \boldsymbol{D}^p \int_{S_i} e^{-ik_p \hat{\boldsymbol{T}}_i \cdot \boldsymbol{r}'} dS_i(\boldsymbol{r}) + \sqrt{\frac{2i\pi}{k_s}}(-ik_s) \sum_{i=1}^{M} \frac{e^{ik_s T_i}}{4\pi\sqrt{T_i}} \boldsymbol{D}^s \int_{S_i} e^{-ik_s \hat{\boldsymbol{T}}_i \cdot \boldsymbol{r}'} dS_i(\boldsymbol{r}). \tag{8}$$

The phase term in 2D can also be expressed explicitly:

$$\int_{S_i} e^{-ik_\alpha \hat{\boldsymbol{T}}_i \cdot \boldsymbol{r}'} dS_i(\boldsymbol{r}) = \sqrt{1 + (\frac{\partial z}{\partial x})^2} l_x \mathrm{sinc}\left[\frac{(k_\alpha \hat{T_{ix}} + k_\alpha \hat{T_{iz}} \frac{\partial z}{\partial x}) l_x}{2} \right] \tag{9}$$

By using these equations and the FFT and its inverse, the received time domain signals are computed explicitly.

III. Numerical Verification

For the transducer excitation we use the Rayleigh integral which is widely used to model the transducer response [2], [13], and the modelling of the source box is proved to be accurate in [14]. Thus the performance of the proposed model mainly depends on the success of the numerical integration across the irregular crack surface. To evaluate the accuracy of this boundary integration, 2D numerical examples with a side-drilled hole (SDH), and a rough crack, are performed and compared with corresponding full FE models.

Fig. 5 illustrates the setup of the FE models for two types of defects. The geometries of the FE models, material properties, and the locations of the defects are the same. The whole rectangular medium is represented by a two-dimensional plane-strain domain bounded by Absorbing Layers with Increasing Damping (ALID) [16]. The size of the total 2D domain is 51.6×37 mm including the absorbing region and the actual area of study is 42.6×28 mm. The defect is first introduced into the model by connecting linear sections to form a solid part, which then is subtracted from the main part domain to create a void. The length of each linear section for a defect is set to be λ_{min}/15, which is sufficiently small to represent the geometry of a typical defect [17]. Points closely surrounding the defect in Fig. 5 denote the monitoring points attached at the surface of the defect. Disconnecting nodes can also create a crack with an arbitrary shape but it is not implemented in the examples shown in this paper. Linear triangular elements (equivalent to CPE3 in Abaqus) with the material properties of aluminium (Youngs modulus, 70GPa; density, 2700 kg/m3; and Poissons ratio, 0.33) are used to mesh the whole domain. With a proper partition, only the region surrounding the defect is meshed via an automatic algorithm and the rest of the domain can be regularly meshed. The element size is approximately λ_{min}/30, well below the conventional limiting size [17].

As can be seen from Fig. 5a, a SDH with a radius of 2mm is placed at the center and a point source is located 20mm away from the centre of the defect at 30^o with respect to the z-axis. It excites a purely P-wave train illuminating the defect with an incident angle of 30^o. A set of boundary monitoring nodes is selected at the defect surface to record the boundary displacement. These displacement time traces are transformed into the frequency domain by FFT and then substituted into Eq. (8) to obtain the far field response at a 20mm distance with the scattering angle ranging from -90^o to 90^o. These frequency values are synthesized back to the time domain by performing an inverse FFT. As a comparison, a semi-circle of monitoring nodes is selected exactly at the required far field points to record the time traces computed from the direct simulation by the FE model. The model is excited with a Hanning windowed tone burst centered at 4MHz fed into the point source. The Abaqus explicit solver is used in this section for 2D models. The snapshot in Fig. 5b shows the scattering waves from a SDH. Later arrivals of both P- and S-waves from creeping waves can be clearly seen after the reflected P- and S-wave main pulses.

Fig. 6 shows the received signals at the specular direction calculated using the boundary integration and the corresponding full FE results. The scattering amplitude is normalized by the peak value of the incident wave. Excellent agreements can be found for both P- and S-waveforms compared with the results from the complete FE model. The integration method also captures the later arrivals from creeping waves well, as the zoom-in plots show. This agreement applies for all the scattering angles monitored from -90^o to 90^o.

As mentioned in Sec. II, it is important to perform integration across the whole contour of the crack since the boundary values of total displacement are used here. An attractive approximation would be to calculate the integration only across the semi-circle facing the source, thus making the shadowing assumption to the other semi-circle, as is normally used by the Kirchhoff approximation [2]. However, the later arrival will not be calculated accurately, as presented in the zoomed plots in Fig. 7, although the main pulse of the first arrivals is still modelled well. This is because the first arrival is the reflected wave contributed from the semi-circle which is illuminated by the incident wave, and the boundary displacements over this semi-circle are all recorded and utilized in the boundary integration. In contrast, later arrivals come from creeping waves which travel across the whole surface of the circle. At the shadowing semi-circle the travelling creeping waves are not recorded and taken into the integration. As a result, the lack of information about creeping waves within the shadowing region leads to the errors of calculated later arrivals. This numerical analysis suggests that taking the boundary integration of only the illuminated surface of the crack will not affect the main reflected waves but may miss the later arrivals.

Fig. 8 shows the comparison of the scattering coefficient for both P- and S-waves at different scattering angles ranging from -90^o to 90^o. The scattering coefficient is defined as the peak amplitude of the Hilbert transformed time domain signals . Good agreement is seen at all scattering angles. The numerical error averaged over all angles is 0.6% for the case of P waves and 0.9% for the case of S waves.

The same numerical comparisons are performed for a rough crack as shown in Fig. 5(c). The upper surface of the crack is a typical Gaussian surface with a roughness of $\lambda_L/6$ and a correlation length of $\lambda_L/4$, and it is generated using the moving average method [4]. The lower surface is produced by multiplying the upper surface with a sinusoidal smoothing function. Fig. 9 and Fig. 10 show the time domain signals at the specular direction and a near grazing scattering angle for the rough crack. The scattering waveforms for near grazing angle are difficult to interpret although two shear wave packets contributed mainly from the two tips as is roughly seen in Fig. 10(b). Good agreement of the waveforms with results from the corresponding FE model is found, indicating that the boundary integration captures the later arrivals from surface waves and tip diffraction with high fidelity. This agreement applies to all other scattering angles. The comparisons of the peak values of the time domain displacement over different scattering angles are presented in Fig. 11. Good agreements are found for both types of waves. The mean error from all angles is just 1.2 % for the P wave model and 0.7 % for the S wave model. The maximum amplitude in Fig. 11 lies at the specular direction or near specular direction, but the displacement values have a wider spread unlike the case with a smooth crack. The scattering field from a smooth crack has a very narrow main lobe at the specular direction. This wide spread is caused by the fact that the roughness redistributes the scattering energy across all scattering angles.

Numerical verification for a complex defect in 3D is not performed in this section because the reference full FE model in 3D is very computationally expensive. However, once the element size and the triangular facet is sufficiently small, the boundary integration in 3D should converge to the exact result. A 3D practical inspection example is shown in the next section and its accuracy is validated by comparison with the hybrid method used in [14].

IV. Applications

In this section, the proposed boundary integration formula will be included in the whole modeling procedure as described in II-A with the hybrid concept. Two typical ultrasonic inspection scenarios are demonstrated and comparisons are made with other numerical approaches. The efficiency of the boundary integration method is shown for a 3D inspection case.

A. 2D Time-of-Flight

The first application is a 2D 35^o time-of-flight diffraction comparing the response of a smooth crack with that of a rough crack. The set up is illustrated in Fig. 12(a) with the transducers symmetrically placed about the center of the defect. The material properties are the same as those used in Section III. The defect is 4mm long, with a depth of 20mm below the inspection surface and is placed with a small tilt of 5^o. The moving average technique is again used here to generate a rough crack with the roughness of $\lambda_L/6$ and a correlation length of $\lambda_L/4$. The input signal fed into Transducer 1 is a five-cycle tone burst compressional wave train with a center frequency of 4MHz. A spatial Gaussian window is applied across the transducer surface to emulate the beam spread from a real transducer. The scattered waves are received by Transducer 2.

Following the proposed numerical approach in II, the incident wave field from Transducer 1 is calculated by the Rayleigh integral to obtain the required force values at the excitation line. Note that the two tips of the excitation line need to be buried in absorbing regions to absorb any unwanted circular waves generated from the ends of this line. The size of the defect FE box is 16×12 mm and the area excluding the absorbing region is 7×3 mm. Although the size of the FE region can be further reduced because the conventional monitoring box is neglected and the FE region can be shrunk closer to the defect, this 2D pitch-catch example is sufficient to demonstrate the efficiency and the accuracy of the proposed method. The FE calculation inside the defect box is performed by the Abaqus explicit solver and the computed boundary displacement signals across the contour of the crack are used in Eq. (8) to calculate the received signals at Transducer 2. For the purpose of comparison, a corresponding full FE model is also performed to obtain the exact received signals. The size of the full FE model is 51.6×37 mm, which is the same as that used for numerical verification in Section III.

The snapshots of the scattering waves around two different cracks are presented in Fig. 12(c) and (f). The reflected P waves, reflected S waves, and tip diffracted waves are clearly separated with a smooth crack as shown in Fig. 12(c). The surface wave is trapped within the crack surface and is radiated only when it travels to the tip of the crack. In contrast, the scattering field with a rough crack is much more complicated and difficult to interpret as can be seen in Fig. 12(f) due to the feature of the roughness. The incident waves are reflected by each small line section of the crack and scattered in all directions, contributing to a wider distribution of the scattering energy. In addition, the energy of surface waves at the rough surface is no longer trapped as is the case with the smooth crack. Surface waves are scattered in all directions when they hit a surface top or valley with a high gradient.

This understanding helps in the interpretation of the received waveforms shown in Fig. 12(d), (e), (g) and (h). The received P-wave with a smooth crack in Fig. 12(d) has a phase change of 90^o compared with the incident

P-wave shown in Fig. 12(b), as expected. The received S-wave has two main separated wave packets referring to two tip diffracted waves. Some later arrivals are found due to the surface wave converted radiated waves. In contrast, the received scattering P-wave from the rough crack in Fig. 12(g) has a change of the shape compared with Fig. 12(d). This is explained by the fact that the reflected P-wave from line sections aligned at different angles of the rough crack have different shapes and different arrival times as well. As a result they accumulate and form a different shape of the scattering P-waveform. Furthermore, only one wave packet can be seen from Fig. 12(h). This is because the widely spreading reflected shear waves, and even the scattering waves converted from surface waves may all join in the tip signals. Diffracted waves from two tips are therefore no longer separated in this 2D case, indicating that the conventional sizing technique using tip diffractions may break down with such a rough crack. All waveforms show excellent agreements between the current coupled model and the corresponding full FE model, indicating that the proposed boundary integration method in conjunction with the hybrid concept has a good accuracy to model a complete real inspection case.

B. 3D Detection

The second example is a 3D 20^o detection of a 4×4 mm rough crack as shown in Fig. 13(a). The inspection setup is similar to the case in 2D and the crack is embedded 20 mm away from the transducer and it is rotated by 20^o with respect to the inspection surface. The material properties of the bulk media are the same as the parameters used in the 2D example. The upper surface of the crack is generated by the 2D moving average method with a roughness of $\lambda_L/8$ and a correlation length of $\lambda_L/2$, and the lower surface is produced by multiplying a sinusoidal function to smooth the upper surface. Both surfaces are created by combinations of many triangular facets and are joined together to form an open crack as shown in Fig. 13(b). The 3D defect box has dimensions of $10.8\times10.8\times10.8$ mm, and the area excluding the absorbing region is about $6\times6\times6$ mm. The 3D meshing of this FE box is produced by a mix of an automatic meshing algorithm and a regular meshing algorithm. A small region closely surrounding the crack is free-meshed first, using a linear tetrahedron element (equivalent to C3D4 in Abaqus). The node and element information is imported to a Matlab code, which is run to grow a regular mesh using the same element type to fill up the remaining portion of the defect FE box. Fig. 13(c) shows the final mesh around the crack and it should be noted here that at the boundary of the free meshing and the regular meshing regions, the two neighbouring elements need to have the same hypotenuse to make the mesh compatible. A big advantage of this combined mesh is that it takes the benefit of the regular mesh and also makes use of the robust capability of free mesh to catch the geometry of the complex defect. The element size is chosen to be $\lambda_L/20$. The recently developed Stiffness Reduction Matrix (SRM) absorbing region [18] is applied here to reduce the thickness of the absorbing region from conventional $3\lambda_{max}$ to $1.8\lambda_{max}$. This results in a significant reduction of the size of the FE defect box. A Hanning windowed five cycle tone burst P-wave signal with a center frequency of 4MHz is applied to Transducer 1 and the scattering waves are received by Transducer 2.

Following the proposed numerical procedure, the incident wave field is calculated by the Rayleigh integral to obtain the force needed at the excitation plane buried in the defect box. FE calculation is performed using the time

domain GPU driven software Pogo [19] to save time. For example, Pogo only needs 31 seconds to solve this typical 3D FE problem with around 1.3 million nodes, which normally takes 30 minutes when using the Abaqus explicit solver. To detect the rough defect, we are mainly concerned with the first main pulse reflected from the crack. According to the numerical study in Section III, using monitoring points located at the illuminated crack surface is sufficient to model the main pulse. The recorded boundary displacements at this surface are then substituted into the boundary integration equation (6) to calculate the received signals at Transducer 2.

The previous hybrid model [14], using a monitoring cube, is implemented here as a reference to compare the accuracy as well as the efficiency with the current method because in 3D, the computational cost is considerably higher for a full FE model. As shown in Fig. 13(d), good agreement is found for the reflected P-wave using both methods. Table 1 presents a comparison of the computation effort between the hybrid method of [14] and the current method. As can be seen, the current method requires substantially fewer monitoring points than the hybrid method. For a typical 3D hybrid problem in [14], three layers of nodes at each surface of the monitoring cube are required because stress components perpendicular to the face are approximated by the first order central difference of the displacement. As a result, a typical monitoring box needs $6\times3=18$ layers of nodes in total to collect near field scattering waves. In contrast, the current method only needs the monitoring nodes placed at the crack surface or the illuminated surface. In other words the monitoring box is minimized so that the number of monitoring signals required is also minimum, which is normally one order less than the hybrid of [14]. The reduction in data required for integration results in a faster post-processing computation.

V. Conclusions

In this paper, a fast and generic finite element (FE) boundary integration coupled modelling tool is developed for elastic wave scattering from complex defects and it is implemented to simulate different real inspection cases. Although several time domain hybrid methods in the NDE area have been developed in the literature [13], [14], the proposed model has advantages of reducing computation cost for both the FE calculation and the post-processing, especially in 3D. By shrinking the monitoring contour into the crack surface itself, the number of monitoring signals is as small as possible and the size of the defect FE box can be reduced as well. We validate the boundary integration across complex surfaces of the defect by comparison with the corresponding full FE models and an excellent agreement within 2% is obtained. One current limitation with the method is that it only works in homogeneous and isotropic materials. The model for anisotropic materials is still under development. This method is of particular interest for Monte Carlo simulations with statistically rough cracks because many realizations have to be run to obtain a statistically meaningful scattering field. Future works might include using the proposed method to find the region of validity for the 3D Kirchhoff elastic approximation with different rough cracks via the method of Monte Carlo. In addition, the proposed approach can be easily extended to the study of the elastic wave scattering from rough surface breaking defects.

REFERENCES

[1] J. D. Achenbach, L. Adler, D. K. Lewis, and H. McMaken "Diffraction of ultrasonic waves by penny-shaped cracks in metals: Theory and experiment," *J. Acoust. Soc. Am.*, vol. 66, no. 6, pp. 1848–1856, 1979.

[2] J. A. Ogilvy and I. D. Culverwell, "Elastic model for simulating ultrasonic inspection of smooth and rough defects," *Ultrasonics*, vol. 29, pp. 490–496, 1990.

[3] V. Zernov, L. Fradkin, and M. Darmon, "A refinement of the Kirchhoff approximation to the scattered elastic fields," *Ultrasonics*, vol. 52, pp. 830–835, 2012.

[4] J. A. Ogilvy, "Computer simulation of acoustic wave scattering from rough surface," *J. Phy. D: Appl. Phys.*, vol. 21, pp. 260–277, 1988.

[5] J. A. Ogilvy, "An estimate of the accuracy of the Kirchhoff approximation in acoustic wave scattering from rough surfaces," *J. Phy. D: Appl. Phys.*, vol. 19, pp. 2085–2113, 1986.

[6] E. I. Thorsos, "The validity of the Kirchhoff approximation for rough surface scattering using a Gaussian roughness spectrum," *J. Acoust. Soc. Am.*, vol. 83, no. 1, pp. 78–92, 1988.

[7] P. Rajagopal and M. J. S. Lowe, "Scattering of fundamental shear horizontal guided wave by a part-thickness crack in an isotropic plate," *J. Acoust. Soc. Am.*, vol. 124, no. 5, pp. 2895–2904, 2008.

[8] P. Rajagopal and M. J. S. Lowe, "Short range scattering of the fundamental shear horizontal guided wave mode normally incident at a through-thickness crack in an isotropic plate ," *J. Acoust. Soc. Am.*, vol. 122, no. 3, pp. 1527–1538, 2007.

[9] M. Frehner, S. M. Schmalholz, E. H. Saenger and H. Steeb, "Comparison of finite difference and finite element methods for simulating two-dimensional scattering of elastic waves," *Phys. Earth Planet. Inter.*, vol. 171, no. 1-4, pp. 112–121, 2008.

[10] P. D. Wilcox and A. Velichko, "Efficient frequency-domain finite element modeling of two-dimensional elastodynamic scattering," *J. Acoust. Soc. Am.*, vol. 127, no. 1, pp. 155–165, 2010.

[11] A. Velichko and P. D. Wilcox, "A generalized approach for efficient finite element modeling of elastodynamic scattering in two and three dimensions," *J. Acoust. Soc. Am.*, vol. 128, no. 3, pp. 1004–1014, 2010.

[12] A. Velichko and P. D. Wilcox, "Efficient finite element modeling of elastodynamics scattering with non-reflecting boundary conditions," in *Review of Progress in Quantitative NDE*, vol. 1430, pp. 142–149, 2012.

[13] N. Gengembre, A. Lhemery, R. Omote, T. Fouquet and A. Schumm, "A semi-analytic-FEM hybrid model for simulating UT configurations involving complicated interactions of waves with defects," in *Review of Progress in Quantitative NDE*, vol. 23, pp. 74–80, 2004.

[14] P. Rajagopal, E. A. Skelton, W. Choi, M. J. S. Lowe and R. V. Craster, "A generic hybrid model for bulk elastodynamics, with application to ultrasonic nondestructive evaluation," *IEEE Trans. Ultrason. Ferroelectr. Freq. Control*, vol. 59, no. 6, pp. 1239–1252, 2012.

[15] H. Lawrence, F. Demontoux, J. P. Wigneron, P. Paillon, T. D. Wu, and Y. H. Kerr, "Evaluation of numerical modeling approach based on the finite-element method for calculating the rough surface scattering and emission of a soil layer," *IEEE Geosci. Remo. Sens. Lett.*, vol. 8, no. 5, pp. 953–957, 2011.

[16] P. Rajagopal, M. Drozdz, E. A. Skelton, M. J. S. Lowe and R. V. Craster, "On the use of absorbing layers to simulate the propagation of elastic waves in unbounded isotropic media using commercially available finite element packages," *NDT & E Int.*, vol. 51, pp. 30–40, 2012.

[17] M. B. Drozdz, "Efficient finite element modelling of ultrasound waves in elastic media," *Phd thesis*, Imperial College London, 2008

[18] J. R. Pettit, A. Walker, P. Cawley and M. J. S. Lowe, "A stiffness reduction method for efficient absorption of waves at boundaries for use in commercial finite element codes," *Ultrasonics*, In Press, 2013.

[19] P. Huthwaite, "Accelerated finite element elastodynamic simulations using the GPU," *J. Comp. Phys*, vol. 257, pp. 687–707, 2014.

Figure & Table captions

Fig. 1. Illustration of the hybrid model used in [14] to simulate a general ultrasonic inspection problem. Step 1: transducer sending signals. Step 2: defect scattering. Step 3: transducer receiving signals.

Fig. 2. Illustration of the model used in this paper to simulate a general ultrasonic inspection problem. Step 1: transducer sending signals. Step 2: defect scattering. Step 3: transducer receiving signals.

Fig. 3. Discretization of the surface of a 3D crack and the corresponding vectors.

Fig. 4. Discretization of a 2D crack and the corresponding vectors.

Fig. 5. Snapshots of the wave propagation and scattering from a SDH or from a rough crack. (a) Propagating P waves from a point source. (b) Scattering waves from the SDH. (c) Scattering waves from the rough crack.

Fig. 6. Comparison of the scattering signals for a SDH from the boundary integration and the complete FE model when the scattering angle is 30^o (specular direction). (a) P-P case. (b) P-S case.

Fig. 7. Comparison of the scattering signals for a SDH from the boundary integration using only the illuminated surface and the complete FE model when the scattering angle is 30^o (specular direction). (a) P-P case. (b) P-S case.

Fig. 8. Comparison of the scattering coefficient across all scattering angles for a SDH. (a) P-P case. (b) P-S case.

Fig. 9. Comparison of the scattering signals for a rough crack from the boundary integration and the complete FE model when the scattering angle is 30^o (specular direction). (a) P-P case. (b) P-S case.

Fig. 10. Comparison of the scattering signals for a rough crack from the boundary integration and the complete FE model when the scattering angle is -80^o (near grazing direction). (a) P-P case. (b) P-S case.

Fig. 11. Comparison of the scattering coefficient across all scattering angles for a rough crack. (a) P-P case. (b) P-S case.

Fig. 12. 35^o time of flight inspection of a smooth crack and a rough crack: (a) Inspection setup. (b) Incident P-wave. (c) Snapshot of scattering waves from a smooth crack. (d) Received scattering P-wave from a smooth crack. (e) Received scattering S-wave from a smooth crack. (f) Snapshot of scattering waves from a rough crack. (g) Received scattering P-wave from a rough crack. (h) Received scattering S-wave from a rough crack.

Fig. 13. 20^o detection of a 3D rough crack: (a) Inspection setup. (b) 3D rough crack. (c) Slice view of the 3D mesh in the defect FE box. (d) Received scattering P-wave.

Table 1. Comparison of the computation effort for post-processing using the previous hybrid method, [14], and the current method.

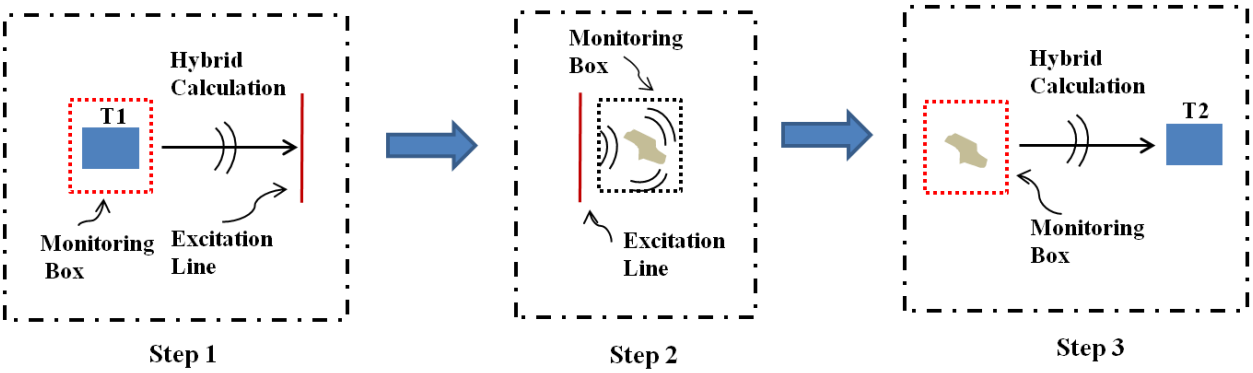

Fig. 1. Illustration of the previous hybrid model [14] to simulate a general ultrasonic inspection problem. Step 1: transducer sending signals. Step 2: defect scattering. Step 3: transducer receiving signals.

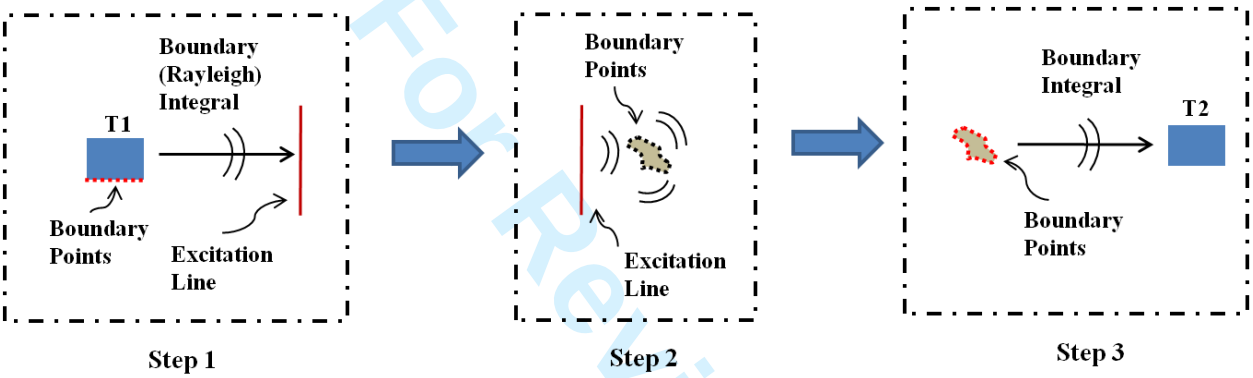

Fig. 2. Illustration of the model used in this paper to simulate a general ultrasonic inspection problem. Step 1: transducer sending signals. Step 2: defect scattering. Step 3: transducer receiving signals.

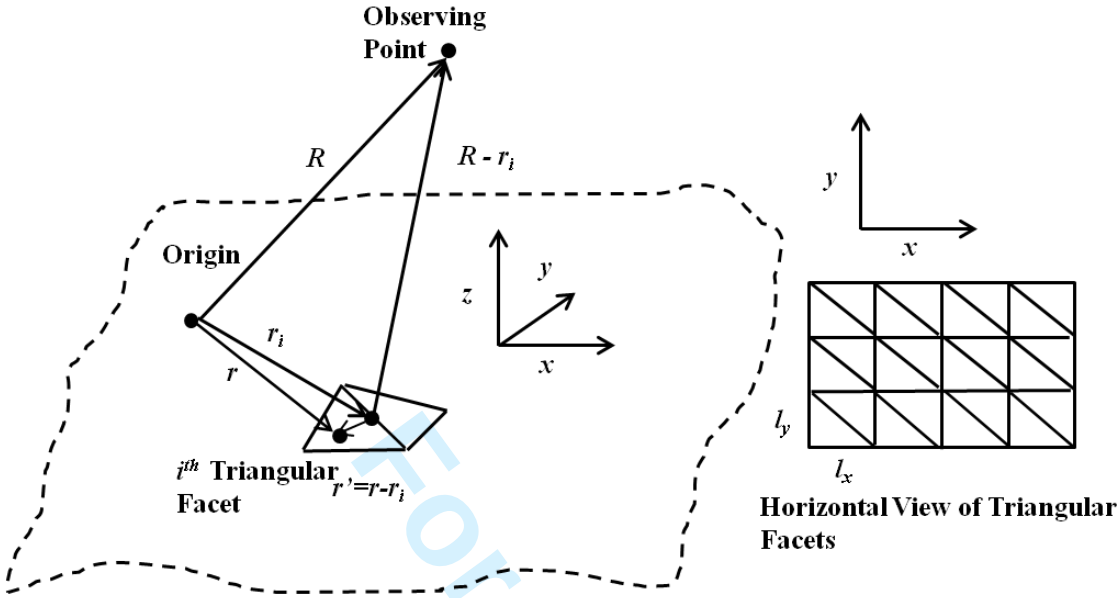

Fig. 3. Discretization of the surface of a 3D crack and the corresponding vectors.

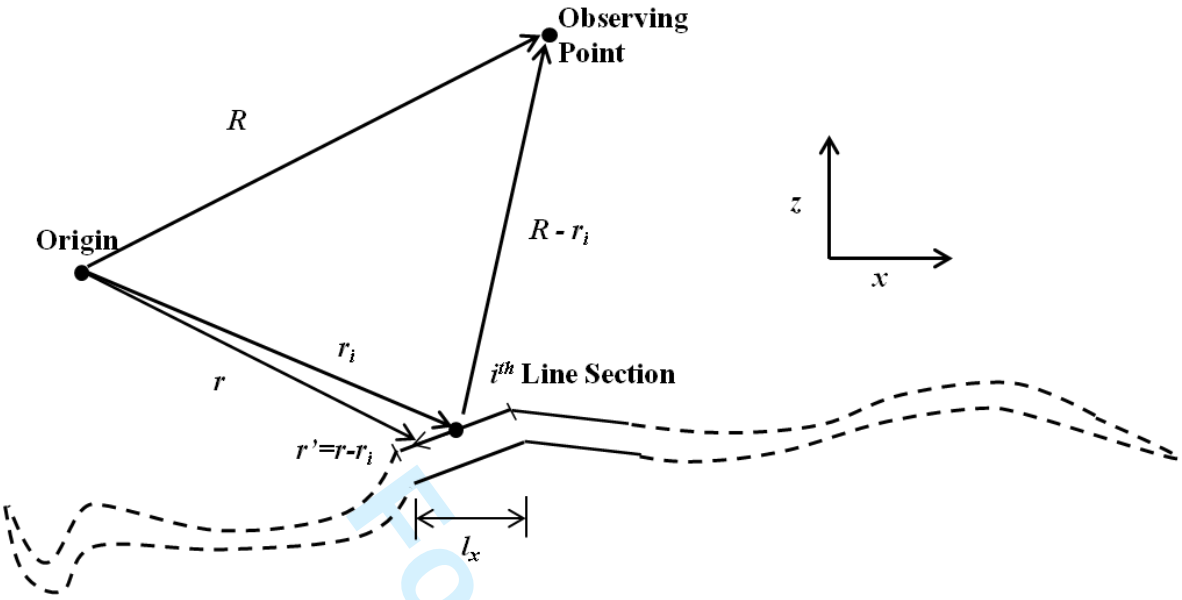

Fig. 4. Discretization of a 2D crack and the corresponding vectors.

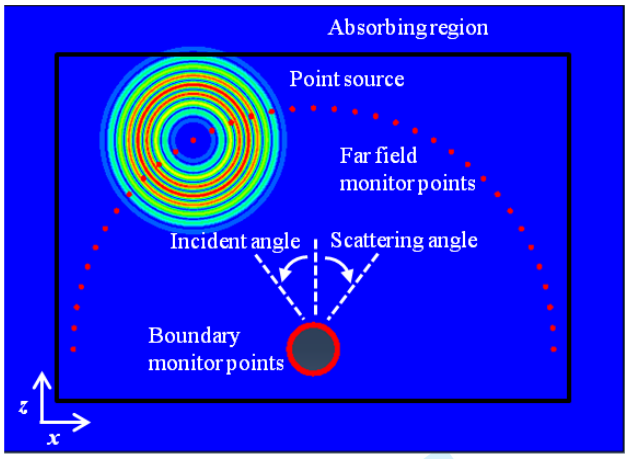

(a)

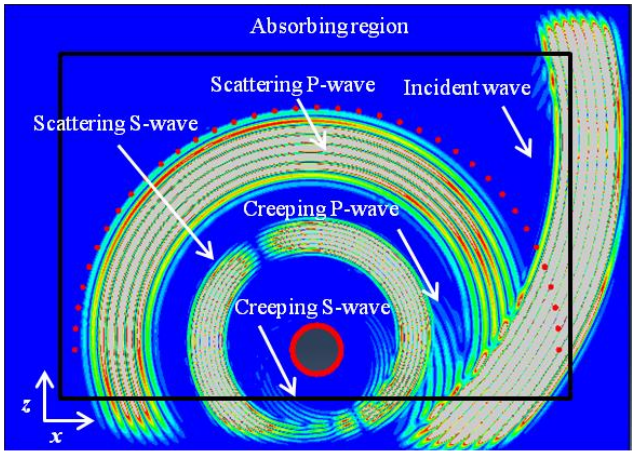

(b)

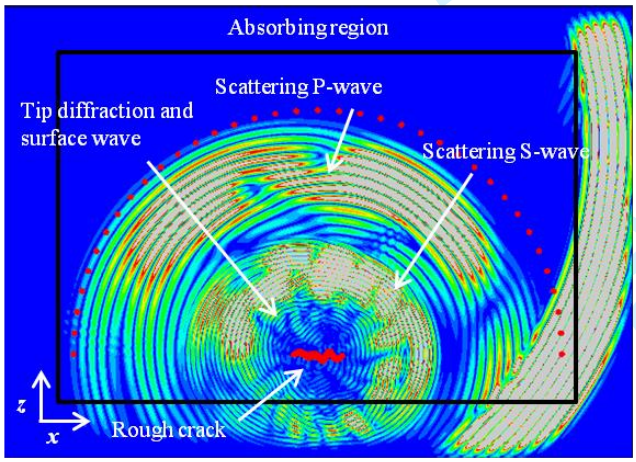

(c)

Fig. 5. Snapshots of the wave propagation and scattering from a SDH or from a rough crack. (a) Propagating P waves from a point source. (b) Scattering waves from the SDH. (c) Scattering waves from the rough crack.

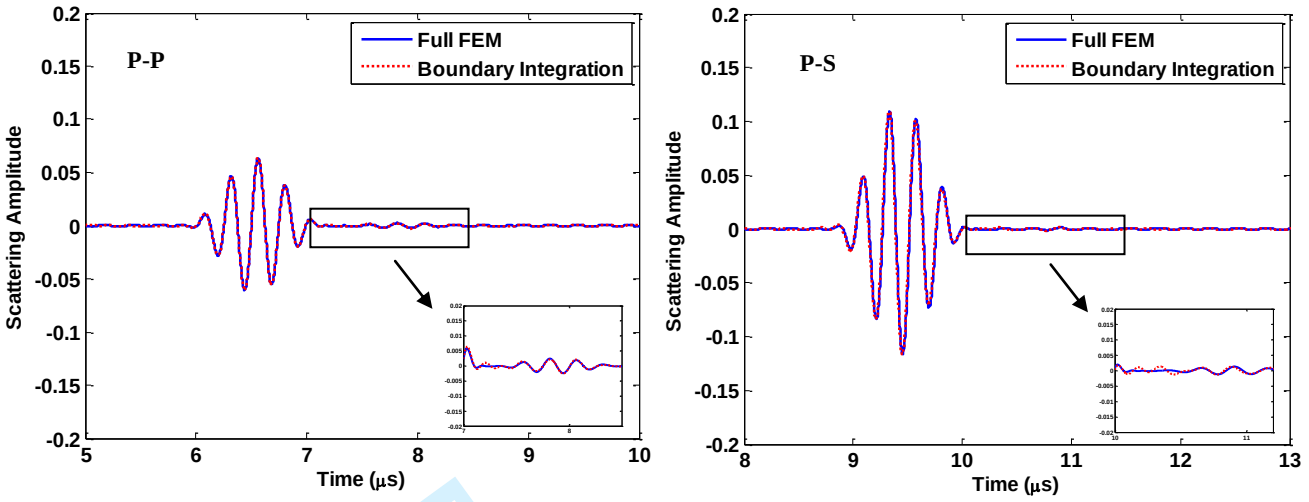

(a) (b)

Fig. 6. Comparison of the scattering signals for a SDH from the boundary integration and the complete FE model when the scattering angle is 30º (specular direction). (a) P-P case. (b) P-S case.

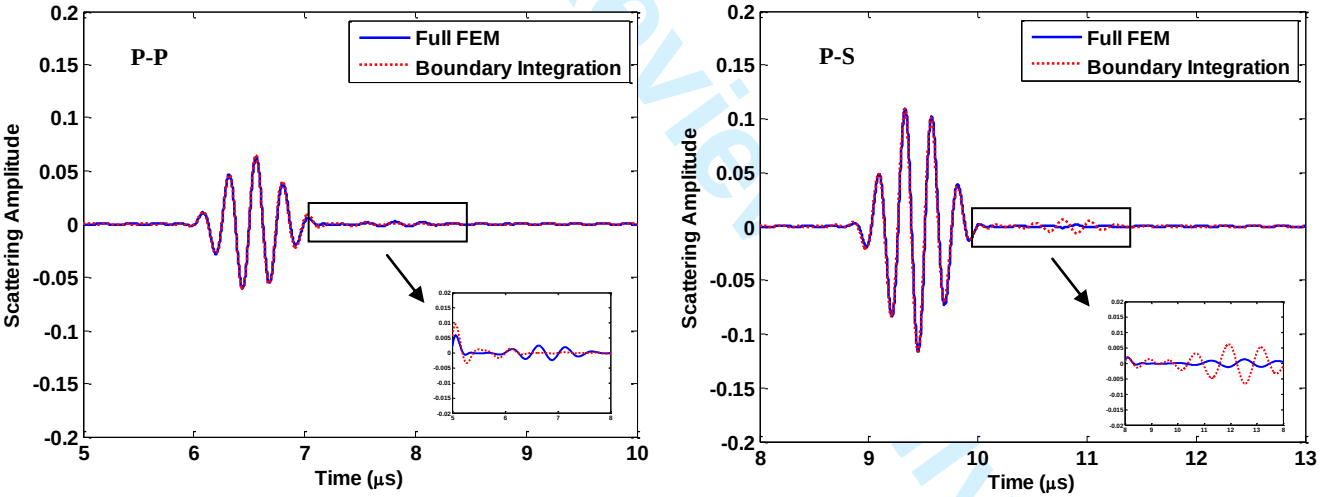

(a) (b)

Fig. 7. Comparison of the scattering signals for a SDH from the boundary integration using only the illuminated surface and the complete FE model when the scattering angle is 30° (specular direction). (a) P-P case. (b) P-S case.

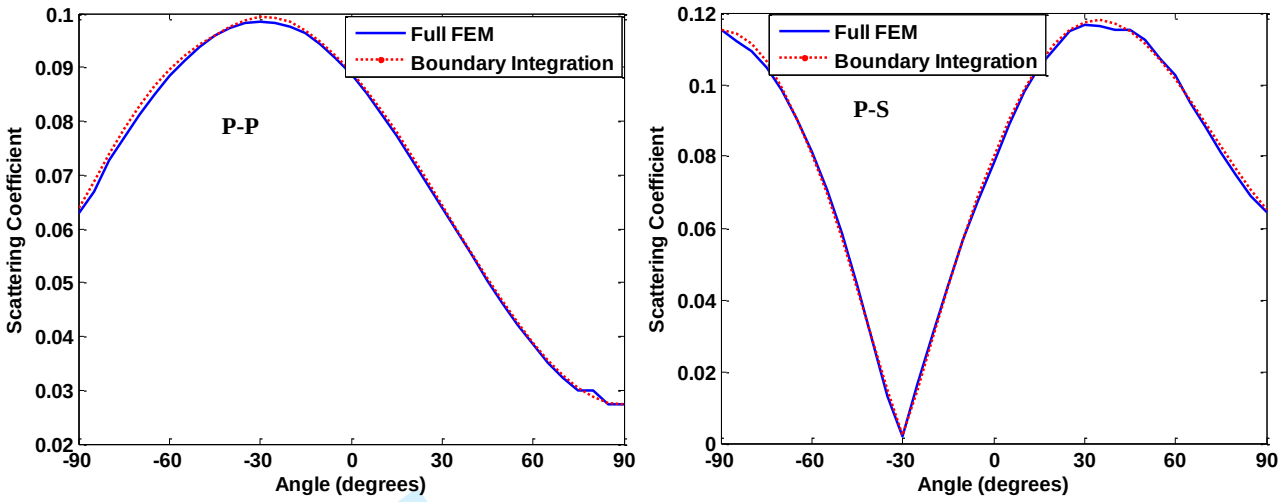

(a) (b)

Fig. 8. Comparison of the scattering coefficient across all angles for a SDH. (a) P-P case. (b) P-S case.

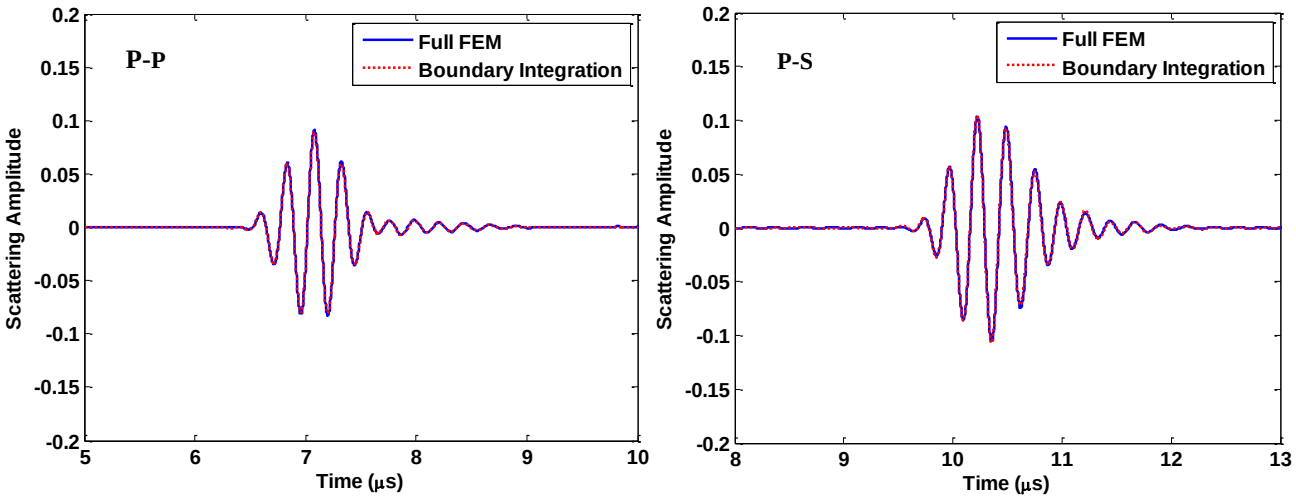

Fig. 9. Comparison of the scattering signals for a rough crack from the boundary integration and the complete FE model when the scattering angle is 30º (specular direction). (a) P-P case. (b) P-S case.

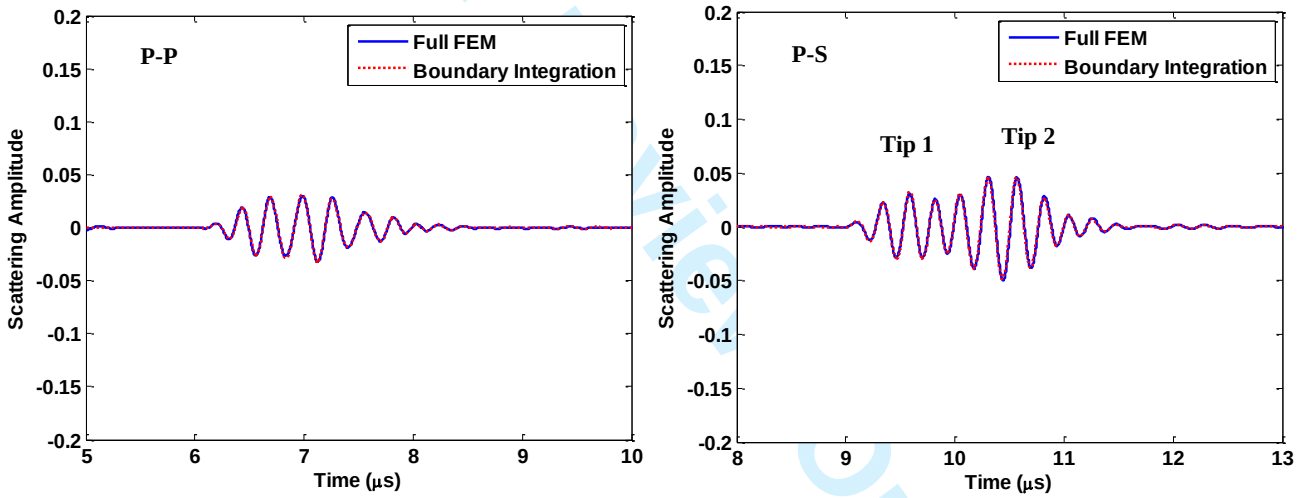

Fig. 10. Comparison of the scattering signals for a rough crack from the boundary integration and the complete FE model when the scattering angle is -80° (near grazing direction). (a) P-P case. (b) P-S case.

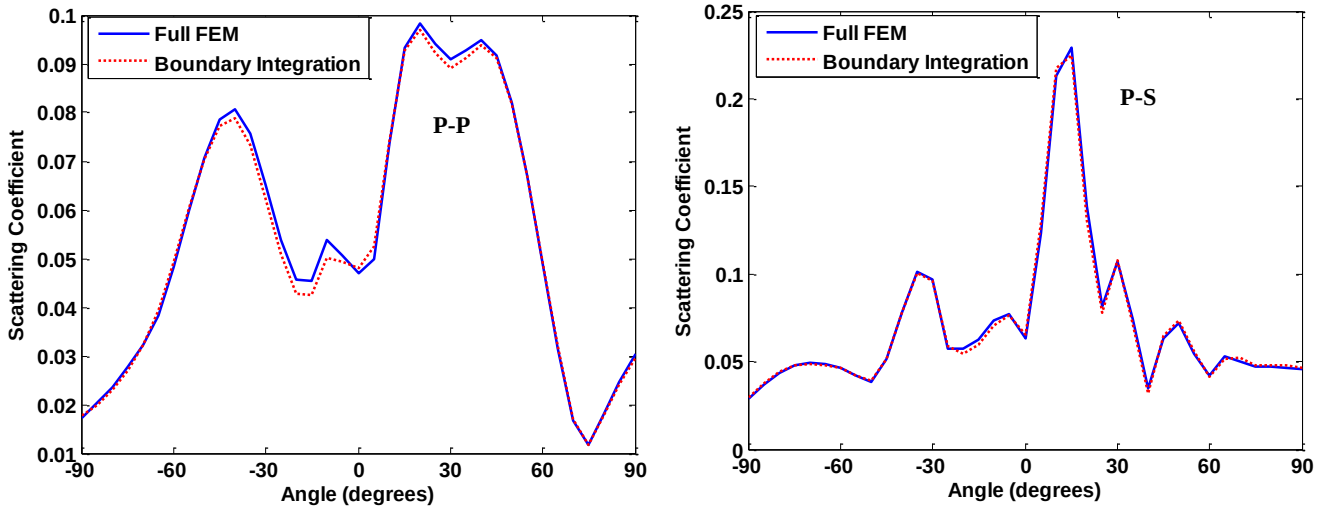

Fig. 11. Comparison of the scattering coefficient across all scattering angles for a rough crack. (a) P-P case. (b) P-S case.

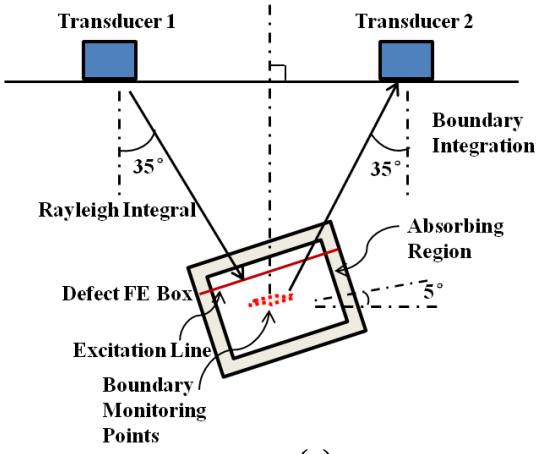

(a)

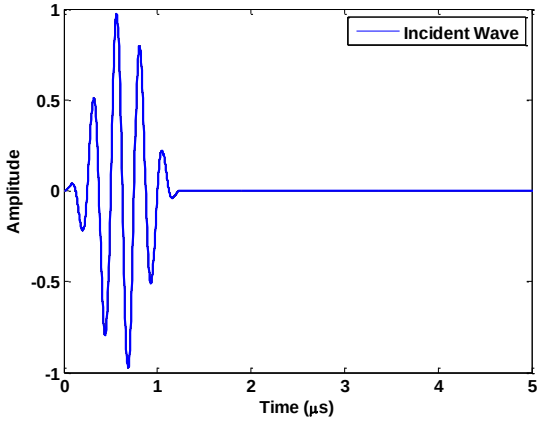

(b)

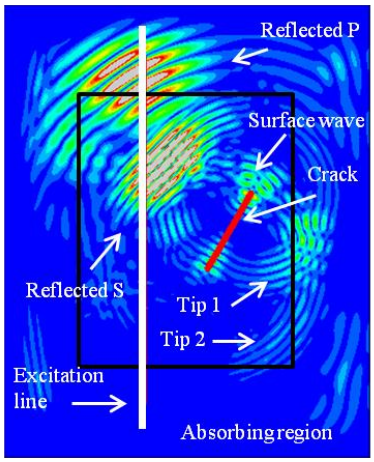

(c)

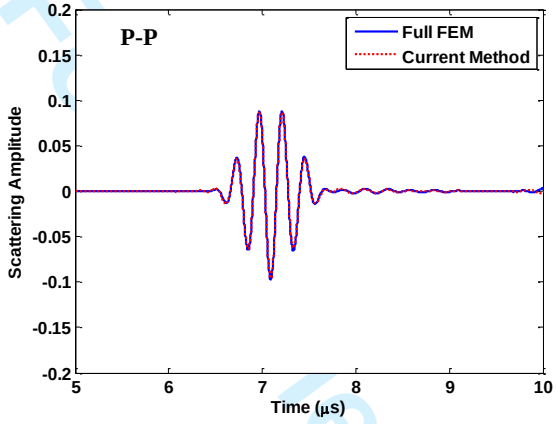

(d)

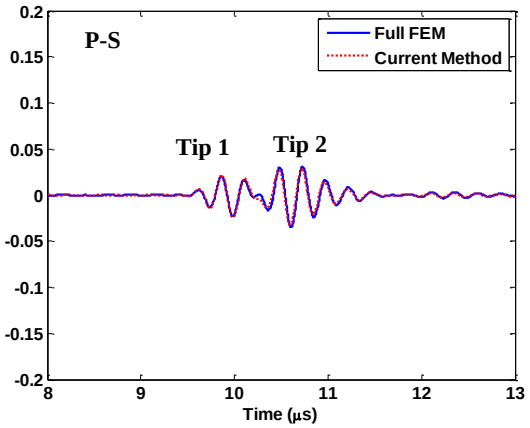

(e)

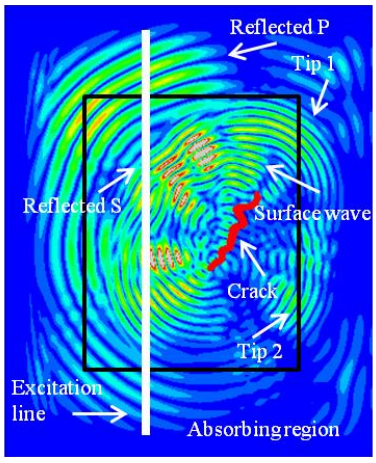

(f)

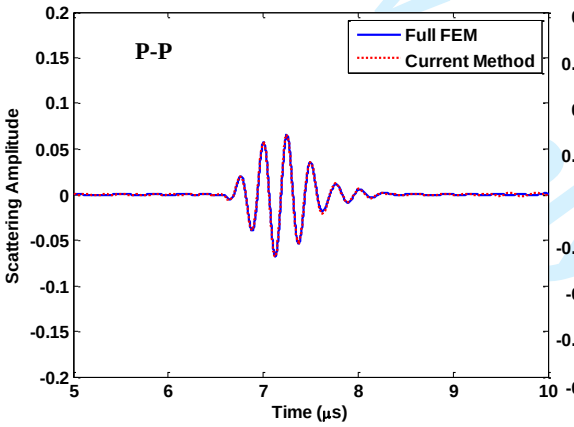

(g)

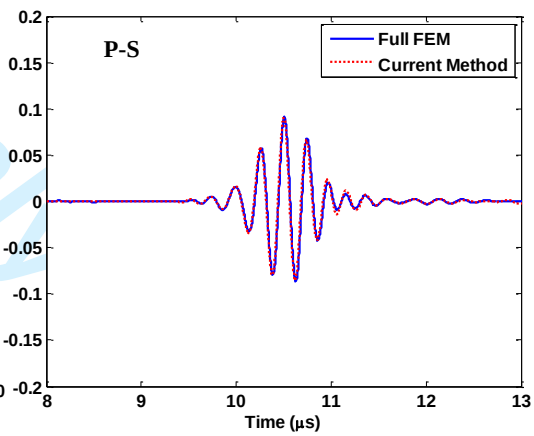

(h)

Fig. 12. 35° time of flight inspection of a smooth crack and a rough crack: (a) Inspection setup. (b) Incident P-wave. (c) Snapshot of scattering waves from a smooth crack. (d) Received scattering P-wave from a smooth crack. (e) Received scattering S-wave from a smooth crack. (f) Snapshot of scattering waves from a rough crack. (g) Received scattering P-wave from a rough crack. (h) Received scattering S-wave from a rough crack.

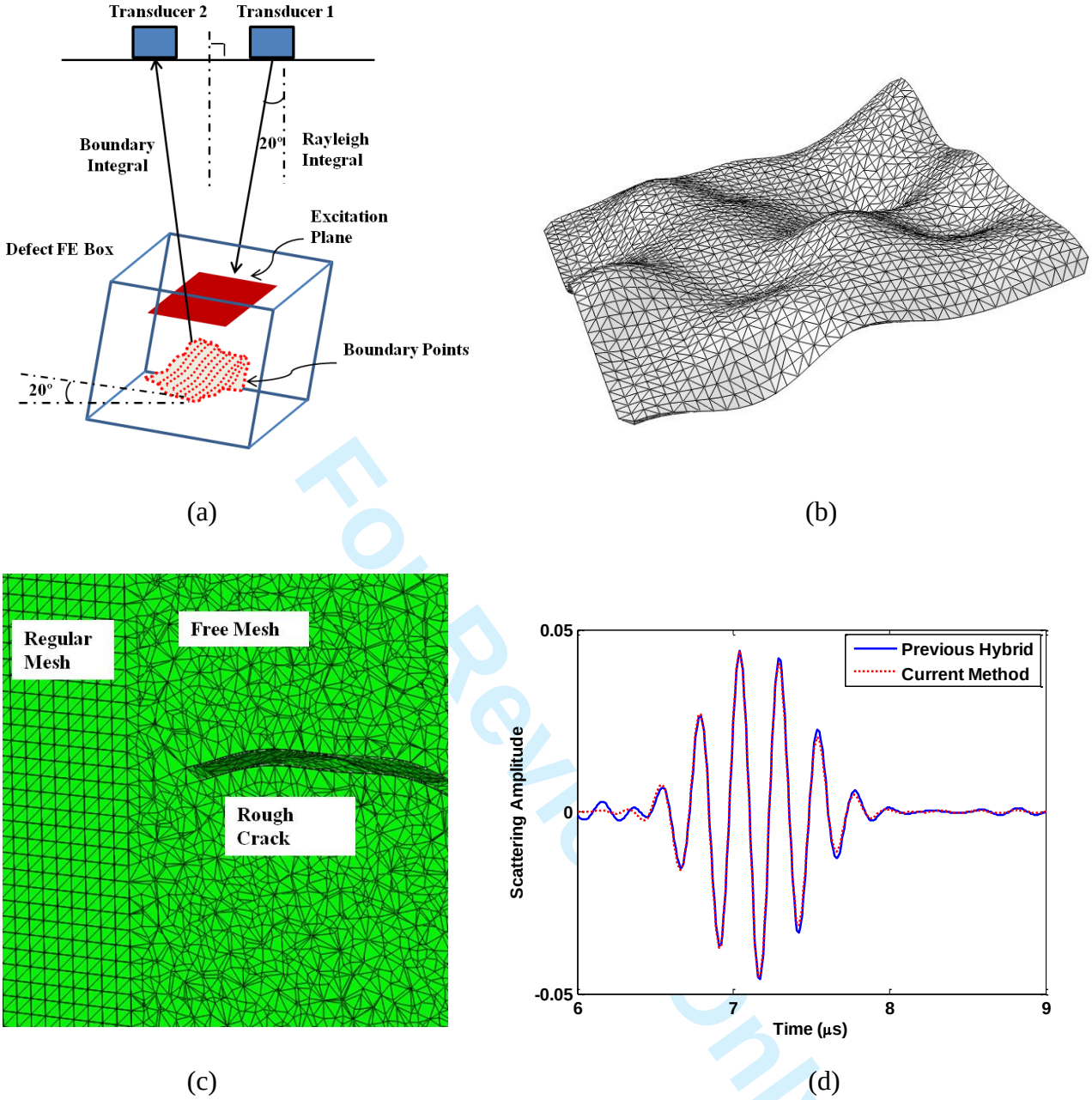

Fig. 13. 20° detection of a 3D rough crack: (a) Inspection setup. (b) 3D rough crack. (c) Slice view of the 3D mesh around the crack in the defect FE box. (d) Received scattering P-wave.

	Number of Monitoring Points	Post-processing Time
Previous Hybrid	2809×6×3 = 50562	457 sec
Current Method	1677	12 sec

Table 1. Comparison of the computation effort for post-processing using the previous hybrid method, [14], and the current method.